Unveiling the role of surface Ir-oxo specie in O_2 evolution at IrO_2 electrocatalyst via embedded cluster multi-reference calculations

Francesca Fasulo,[1] Abhishek Mitra,[2] Ana B. Muñoz-García,[1] Michele Pavone,[3,*] and Laura Gagliardi[2,*]

[1]*Department of Physics "E. Pancini", University of Naples Federico II, Comp.Univ. Monte Sant'Angelo, Via Cintia 21, Naples 80126, Italy*

[2]*Department of Chemistry, Pritzker School of Molecular Engineering, University of Chicago, Chicago, 5735 S Ellis Ave, Chicago, IL 60637, USA*

[3]*Department of Chemical Science, University of Naples Federico II, Comp.Univ. Monte Sant'Angelo, Via Cintia 21, Naples 80126, Italy*

***Corresponding authors: michele.pavone@unina.it, lgagliardi@uchicago.edu**

ABSTRACT

Understanding the mechanisms driving the oxygen evolution reaction (OER) on iridium oxide (IrO_2)-based catalysts is essential to improve their performance and enable an actual scale-up of water splitting photoelectrochemical cells. The OER mechanistic pathways at IrO_2 interfaces have been extensively investigated computationally using density functional theory (DFT), which predicts a high energy barrier for the OER last step of molecular oxygen detach and release from the catalyst surface. Nevertheless, surface-O_2 over- and under- binding results by standard GGA and hybrid density functionals, respectively, call for further analysis of this crucial step via multireference methods. Aiming at unveiling the nature of such barrier, we hereby address the formation of O_2 from the most stable IrO_2(110) surface with both periodic DFT and an electrostatic embedded cluster approach at the n-electron valence state perturbation theory (NEVPT2). With this multireference approach we find a value for the aforementioned energy barrier that is much closer to experimental indications than DFT ones. An in-depth analysis of the involved molecular orbitals suggests that the origin of this barrier is related to the breaking of a π interaction between O_2 and Ir surface atom, and to a significant additional O_2 interaction with adjacent electrophilic Ir-oxo specie, which is present under experimental operating conditions. Besides shedding light on the OER mechanism on IrO_2, these findings point out the importance of multireference methods for dissecting complex reactions at electrocatalytic interfaces and pave the route for further investigations with effective embedding approaches.

INTRODUCTION

Iridium oxide (IrO_2) is the current benchmark electrocatalyst for oxygen evolution reaction (OER) in water-splitting devices targeting hydrogen production, due to its low overpotential and great corrosion resistance under acidic conditions.[1] However, the high costs and limited global supply of iridium-based materials have called for design of new OER electrocatalysts. Understanding IrO_2 stability and mechanisms driving the OER is thus essential to identify and optimize alternative Ir-free catalysts and achieve an efficient scale-up of water-splitting technologies. Three possible mechanisms are commonly proposed for the OER on IrO_2: the adsorbate evolving mechanism (AEM), the oxo-coupling mechanism (I2M) and lattice oxygen mechanism (LOM) (Scheme 1).[1-3] In all proposed paths, the active site is the Ir-oxo specie generated by oxidation of adsorbed water molecules. These species, with a radical character and electron deficiency[4-6], were found as an intermediate for electrochemical and thermal iridium oxide anodes.[5] When the iridium oxide nanoparticles are full oxidated, with large concentration of surface Ir-oxo species, the OER release is enhanced,[4] thus suggesting the Ir-oxo species can have a direct role in catalyzing the OER.[4] The AEM path implies the formation of an hydroperoxo species (Ir-OOH) and a proton coupled electron transfer step (PCET) before O_2 release, while the O-O bond is formed by the coupling of Ir-oxo species with an adjacent Ir-oxo or a lattice oxygen atom (O_{lat}) in the I2M and LOM, respectively. Previous density functional theory (DFT) investigations have suggested that the OER takes place preferentially via the AEM mechanism at the most exposed IrO_2 facet, i.e. the (110), and less stable (100), (001), (211) surfaces, while the I2M is favoured on the IrO_2(011) surface, and the formation of metal vacancies with catalyst dissolution can lead to slightly lower OER overpotentials for the LOM at (110) and (211) facets.[6,8-10] Moreover, atom probe tomography (APT) experiments highlighted an exchange of oxygen atoms in the first 2.5 nm of the rutile IrO_2 lattice, possibly due to OER happening via I2M and LOM.[11]

Scheme 1. *Proposed mechanisms for oxygen evolution at IrO_2 surfaces. From top to bottom: adsorbate evolving mechanism (AEM), oxo-coupling mechanism (I2M) and lattice oxygen mechanism (LOM).*

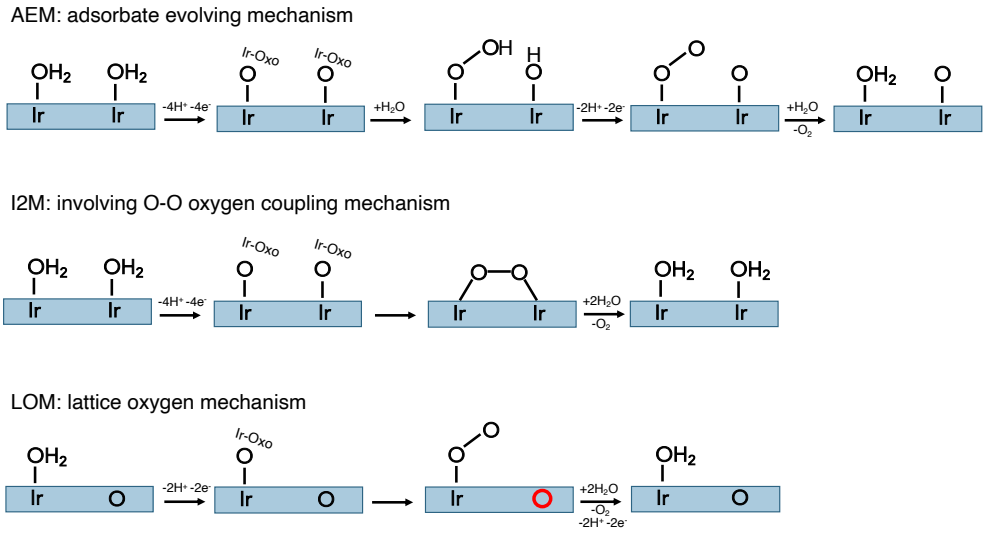

In spite of these findings feeding the debate about whether the LOM and I2M can compete with the AEM, the AEM is accepted as most likely scenario, especially at the most exposed stoichiometric $IrO_2(110)$ facet, due to great stability of IrO_2 under OER conditions[2] and susceptibility of Ir-oxo species to nucleophilic attack[8]. Therefore, the AEM mechanism has been widely studied. [6,8-10] From both periodic DFT [6] and dynamic microkinetic models, based on theoretical and experimental data,[12,13] the deprotonation of adsorbed water molecule (see AEM step 3 in Scheme 1) was identified as the rate-determining step. Besides, detachment of oxygen molecules, which is critical in freeing the catalytic site for subsequent reactions, also demands significant amount of energy. DFT predicts a higher energy barrier for the oxygen release (DFT(PBE) ~0.56/0.58eV) than the experimentally derived microkinetic reference (0.43 eV). [12,13] This can be ascribed to the over-binding of oxygen molecule to surface given by the used semi-local exchange-correlation functional PBE.[14,15] Furthermore, oxygen dissociation from the surface evolves continuously from a doublet state when O_2 is bound to the surface to a triplet dissociated state, with another water molecule not binding to the O vacancy site until O_2 is removed from the surface.[6] This specific step can significantly influence the overall reaction kinetics and efficiency, calling for further investigations using methods beyond DFT to point out the origin of DFT failure for this intermediate, and obtaining a reliable

energy barrier that is consistent with experimentally derived data. By incorporating static and dynamic electronic correlation, multireference methods, such as the n-electron valence state perturbation theory (NEVPT2)[16], can achieve a reliable and more realistic description of radical systems (e.g the electrophilic Ir-oxo active site) and of the oxygen triplet ground state. Indeed, even though DFT is a highly powerful and cost-accuracy advantageous tool for comparing different materials or several possible reaction paths and for prediction of physical-chemical properties of materials[17], common functionals would introduce significant errors (greater than 0.3 eV) into the overall energy for the ORR and OER steps.[18] Plus, while generalized gradient approximation (GGA) and hybrid functionals over- and under- (e.g. heme), respectively, multireference methods are shown to better reproduce the experimental binding energies.[19] Such functional-dependent energetic over- and under- estimations can also affect the characterization of O_2 release, as shown by reported radical O–O coupling reaction in diferrate-mediated water oxidation, where DFT predicts a rather stabilized product state, compared to multireference approaches.[20] With these premises, we hereby report a thorough study on oxygen release from the most stable stoichiometric IrO_2(110) surface by means of electrostatic embedded approach (EEC) based on NEVPT2 level of theory[16] (EEC[NEVPT2]), aiming at obtaining an accurate estimation of oxygen release thermodynamic barrier and unveiling its nature. A cluster of atoms where the localized chemical processes occur is described at NEVPT2 level of theory, while the extended chemical surface environment is simulated through an embedded cluster approach.[21] In particular, we use an electrostatic embedded approach where the cluster is embedded in a point charge field. This strategy has been already demonstrated to be reliable for the description of adsorption processes and complex reactions on metal oxides surfaces.[21-25]

Though the AEM vs I2M and AEM vs LOM are already studied, a full and consistent comparison of the three proposed OER mechanisms at IrO_2(110) interface (Scheme 1) is still lacking in current literature, to the best of our knowledge. In the following, we report for the first time a complete overview of the three mechanisms, the AEM, I2M and LOM, within a slab approach at the PBE-D3(BJ) level of theory (pDFT[PBE]). Concerning the OER mechanism, our results highlight that the AEM and I2M can lead to

the same last two steps for dioxygen evolution. The oxygen molecule release occurs after overcoming a slightly high energy barrier. Correcting the pDFT[PBE] barrier via the EEC[NEVPT2] (pDFT:NEVPT2), we predict a barrier of 0.45/0.47 eV, very close to an experimentally derived microkinetic value (0.43 eV) [12], while a higher barrier is predicted by pDFT[PBE] (0.56/0.58 eV).[6,12,13] Furthermore, the theoretical characterization by multireference methods allows us to dissect the origin of this thermodynamic barrier, due to the breaking of a π interaction between O_2 and Ir surface atom and a further interaction with adjacent electrophilic Ir-oxo species, which are present at experimental operating condition.[6]

METHODS AND COMPUTATIONAL DETAILS

DFT spin-polarized calculations are performed within the supercell approach with periodic boundary conditions (PBC) and plane-wave (PW) basis sets, as implemented in the Quantum Espresso (QE) package.[26] The generalized gradient approximation (GGA) for the exchange-correlation functional proposed by Perdew, Burke and Ernzerhof (PBE)[14,15] are used with the D3(BJ) correction to account for dispersion forces at the interface.[27] Core electrons are described by projector-augmented wave (PAW) potentials from QE repository[28,29], while the valence/outer-core electrons included in the self-consistent-field calculations are: [$5d^7 6s^2$] for Ir, [$2s^2 2p^4$] for O, and [$1s^1$] for H atoms. The wave functions (augmented charge density) are expanded in plane waves with a 55 (220) Ry cutoff. The Methfessel-Paxton sampling method for Brillouin-zone integration of the first order with 0.02 Ry smearing width[30] is used as occupation function due to metallic character of IrO_2. We apply the surface-slab approach[31] to build up the structural models for IrO_2 surface by cleaving the optimized bulk structure (Figure S1a in SI) along the (110) lattice plane and then introducing 20 Å of vacuum along the c direction (Figure S1b in SI). The 2x1 supercell containing 5 layers of IrO_2 (i.e., 20 formula units (f.u.) / 60 atoms) is used for all the reaction intermediates and mechanisms upon O_2 release. On these slabs, we use a 2x2x1 k-point sampling (6x6x8 for IrO_2 bulk) based on the Monkhorst-Pack scheme and take into account dipole correction as implemented in QE.[32] All geometry optimizations are performed relaxing the atomic positions within the two topmost layers of the

IrO_2(110) slab until the maximum forces acting on each atom are below 30 meV/Å, while all the other atomic coordinates are kept constant.

For embedding cluster calculations at NEVPT2 level of theory we mimic the extended crystal via a large point charge array surface (Ir(+4) and O(-2)) by an electrostatic embedding, as implemented in ORCA[34]. We use the def2-TZVP basis set, while effective core potentials (ECPs)[35] are employed for Ir atoms bonded to the terminating O, but not included in the cluster, to avoiding artificial drift of electron density from the anions onto their nearby positive point charges. Cluster size and point charge array appropriate dimensions are discussed in the following Section II.

RESULTS AND DISCUSSION

I. OER at IrO_2(110) facet: periodic DFT

Motivated by the lack of a full and consistent picture of the three proposed OER mechanisms at IrO_2(110) surface (Scheme 1), we computed all the three energetic pathways (AEM, LOM and I2M) using periodic DFT at the PBE-D3(BJ) level of theory (pDFT[PBE]). All considered steps with corresponding energetics are shown in Figure 1. Due to the well-known full oxidation of IrO_2 facets occurring at the operating conditions[4-6], the starting point in all mechanisms ("0" in Fig.1, state 0 in Scheme S1) is the IrO_2(110) surface with a full coverage of Ir-oxo species. The formation of such full oxidated surface, henceforth called (110)-oxo, is highly favored (E_f = -2.57 eV, see Figure S1b in SI). The succeeding steps of the three mechanisms are referred to this state 0 (the (110)-oxo surface), and the relative energies (E_r) are computed as:

$$E_{r1} = E_n - E_{(110)-oxo} - mE_{H2O} \quad (1)$$

$$E_{r2} = E_n - E_{(110)-oxo} - \left(mE_{H2O} - \frac{m}{2} E_{H2}\right) \quad (2)$$

$$E_{r3} = E_n - E_{(110)-oxo} - \left(mE_{H2O} - mE_{H2}\right) \quad (3)$$

where $E_{(110)-oxo}$ and E_n are the electronic energies for the full oxidated (110)-oxo surface and for the minimum-energy structure of the nth step respectively. Eq. 1 (E_{r1}) is used for the OER step of water adsorption (+mH_2O, with m the number of water molecule), while eq. 2 (E_{r2}) and 3 (E_{r3}) are for the first (+H_2O, -H^+-e^-) and second proton-electron transfer (+H_2O, -2H^+-2e^-), respectively. The Scheme S1 and Figure S2 also show the overall studied mechanisms and the energy differences between two successive steps ($\Delta E = E_n - E_{n-1}$), respectively.

By looking at the first step of each mechanism in Figure 1, we find that the dissociative adsorption of a water molecule on top of electrophilic Ir-Oxo species (A0) in AEM has a negative formation energy (-0.61 eV), while the oxo-oxo (I2) and oxo-O_{lat} (L2) coupling require ~0.27 eV and ~0.76 eV, respectively. These results highlight that the electron deficiency of Ir-oxo species makes the oxygen susceptible to nucleophilic attack from another water molecule, which, in turn, is dissociatively adsorbed, favoring the adsorbate-evolving mechanism, in agreement with previous theoretical studies.[6-10] As already known,[6-10] the two successive proton couple electron transfers from A0 to A1 and from A1 to A2 are the rate limiting steps. Regarding LOM, it is the most unlikely scenario, with the highest energy demand for oxygen release ($\Delta E_{L3-L2} \approx 2.93$ eV), probably due to great stability under OER conditions of IrO_2, as suggested by Zagalskaya et al.[8] As for I2M, the oxygen release via the oxo-coupling mechanism can follow different paths from I2: cleavage of both Ir-O_2 bonds (I3, orange path in Figure 1) or only one (I2a, yellow path in Figure 1). The latter requires less energy ($\Delta E_{I2a-I2} \approx 0.79$ eV vs $\Delta E_{I3-I2} \approx 1.81$ eV), and the surface Ir atom is saturated with further adsorption of H_2O, leading to a local minimum, the I2b species (orange box in Figure 1). From this local minimum, the direct oxygen evolution (I2c, starred-violet path in Figure 1) is less favored than the water oxidation (I2b'). Following this path along the I2M, further water oxidation leads to the A2 steps. These findings suggest that the I2M converges to the same last two steps of AEM (A2 and A3) at high potential.

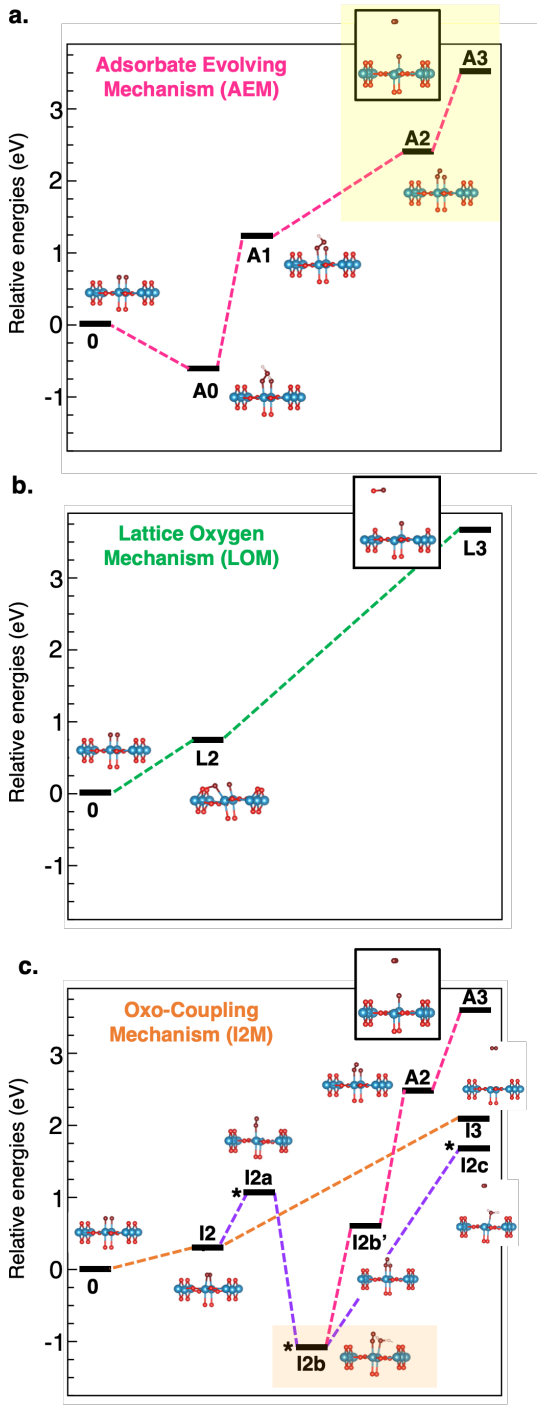

Figure 1. *Minimum-energy structures of the oxygen release paths (Scheme S1 in SI) on top of the full oxidized IrO_2(110) surface, computed at PBE-D3(BJ) level of theory with the corresponding energetics. Color code: AEM (magenta lines), LOM (green lines), I2M (orange/violet lines). Ir (light blue), O_{lat} (red), O_w (dark red), H (pink).*

The A2 to A3 oxygen evolution overcomes a high energy barrier of ~1.10 eV, in agreement with previous theoretical studies ($\Delta E_{A3-A2}(DFT-PBE) \approx 1.00\ eV$).[6] The released molecule at 5Å from the surface (A3) is a triplet dioxygen, as shown by analysis of oxygen bond length ($d_{O\text{-}O}$) and electronic characterizations in Figure S2 and S3 in SI. While the A2 state presents a singlet spin multiplicity with total magnetization close to 0 (0.17 a.u.), the atom- and spin-resolved projected density of states (pDOS) for both states (Figure S3a in SI) reveal a difference between the two spin channels for the A3 state. This finding is confirmed by the spin density (Figure S3b in SI) localized on the O_2 and Ir-oxo species with spin populations of ~$2e^-$ and ~$1e^-$, respectively, resulting in a total magnetization of 3.26 a.u. Motivated by these results and the widely known functional-dependent energetic over- and under-binding of O_2 to metal centers[18-20], we performed further analysis with electrostatic embedding beyond standard DFT for AEM oxygen evolution, in order to achieve a more accurate description of the radical species and released triplet O_2 and obtain a more physically-sound estimate of the energetics involved in the process.

II. Oxygen release via electrostatic embedded approach: method validation

To validate our cluster/environment choices, we compare the energy requirement and electronic features of last AEM step (ΔE_{A3-A2}) computed with periodic boundary conditions and within the embedded cluster framework, both at the DFT-PBE-D3(BJ) level of theory (pDFT[PBE] vs EEC[PBE]). Such comparison has been made for different cluster sizes and shapes, starting from the smallest cluster with only two Ir atoms, named Ir2, and increasing cluster size by adding two Ir atoms of the surface layer. Such an addition can be oriented along the x or y directions, and, accordingly, two different Ir4 clusters can be obtained: Ir4,x and Ir4,y. Further inclusion of one Ir atom on the subsurface layer of IrO_2(110) surface delivers the Ir5,x and Ir5,y clusters, respectively. Finally, cluster Ir7 includes both 2 Ir atoms along both x and y direction plus a subsurface Ir. All clusters considered are collected in Figure 2a. Concerning charge arrays (Fig. 2b), we consider two possibilities for each cluster defined above, one containing ~3800 point charges (Env-1), and one 10Å and 5Å larger in the x- and y- direction than Env-1 (called Env-2) for a total of ~7100 charges.

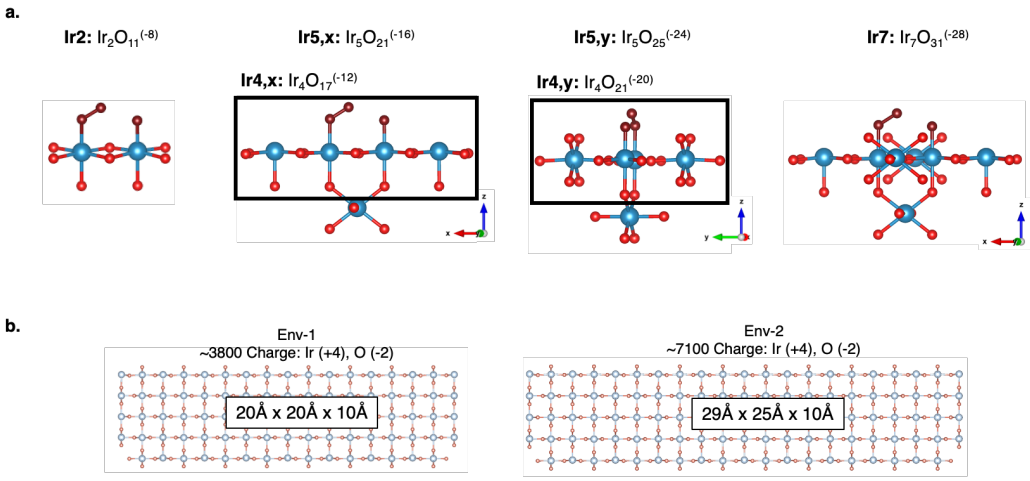

Figure 2. a) *Cluster and* ***b****) point charge arrays of different size carved from periodic (110)-IrO_2 surface. The clusters are named as Ir(n), where n is the number of Ir atoms. To the smallest cluster Ir2, 2 Ir atoms can be added toward x or y direction, lead to Ir4,x and Ir4,y. Further inclusion of one Ir atom on the bottom layer gives the Ir5,x and Ir5,y, respectively. Finally, cluster Ir7 include 2 Ir atoms toward both x and y and the one bottom Ir. Concerning the charge array, Env-2 is 10Å and 5Å larger in the x- and y- direction, respectively, with regards to Env-1. Atomic color code: as Figure 1.*

Table 1. *Energy difference between A2 and A3 states ($\Delta E_{A3\text{-}A2}$) for different-size clusters (Fig. 2a) with the two charge arrays in Fig. 2b at PBE-D3(BJ) level of theory. The pDFT refers to the periodic DFT[PBE-D3(BJ)] barrier.*

$\Delta E_{A3\text{-}A2}$ (eV)	Ir2	Ir4,x	Ir4,y	Ir5,x	Ir5,y	Ir7	pDFT
Env-1	1.67	0.95	1.22	1.13	1.05	1.20	1.10
Env-2	1.01	1.17	1.23	1.30	1.00	1.14	

Detailed analysis on ΔE_{A3-A2} (Table 1) reveals that the charge array size has a significative effect only for the smallest cluster. In particular for Ir2, the energy barrier decreases by 0.66 eV when moving from Env-1 to Env-2, while the variation for larger clusters is smaller than ~0.2 eV. Overall, considering the largest

Env-2, the computed energy differences for all the clusters in Figure 3 agree with the reference periodic PBE-D3(BJ) result (pDFT in Figure 3, 1.10 eV). Concerning the electronic structures for clusters in Env-2, relevant spin features calculated at the PBE-D3(BJ) level of theory (spin density, and the spin number S_z) are collected in Figure 3, in comparison with the total magnetization for the periodic system computed as the difference between spin up and spin down electrons ($\Delta S_{up-down}$). By definition, S_z is half of periodic total magnetization $\Delta S_{up-down}$. The embedded cluster method delivers an increasing number of unpaired electrons with increased cluster size. This behavior derives from the metallic nature of the IrO_2 surface that we divide in a cluster and in a point charge array, and the use of localized basis set, so that a further localization of Ir electron occurs. Thus, we infer that the Ir2 cluster shows the best agreement with electronic structure of the periodic surface.

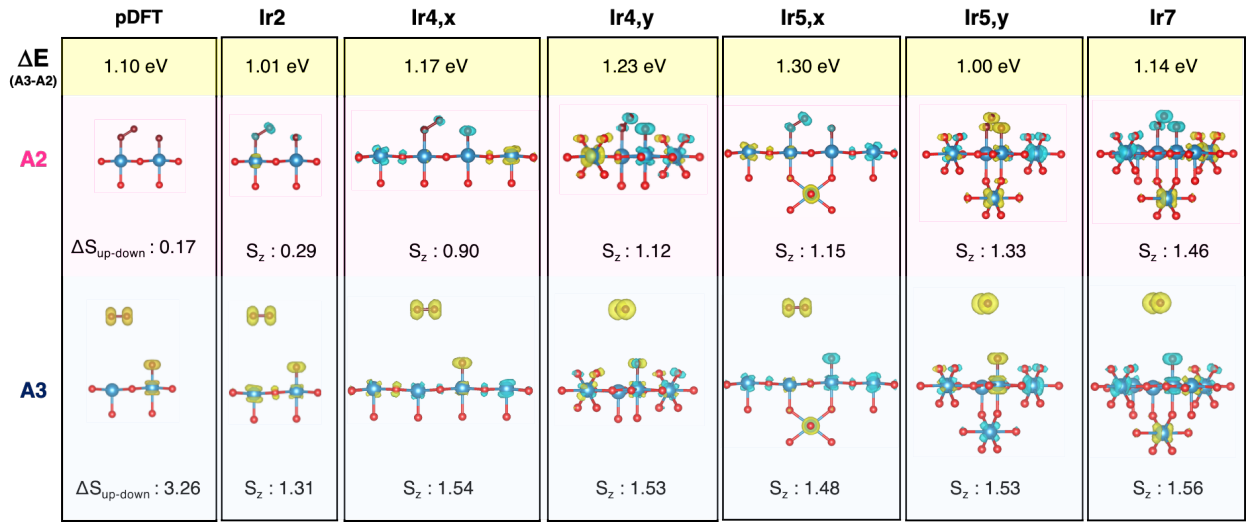

Figure 3. *Energy difference between A2 and A3 steps of the AEM and spin density with total magnetization ($\Delta S_{up-down}$) for periodic system (named pDFT) and with the spin number S_z for embedded clusters of A2 and A3 state at PBE-3(BJ) level of theory. Isosurface 0.03 a.u. Color code: as Figure 1; spin up (yellow), spin down (cyan)*

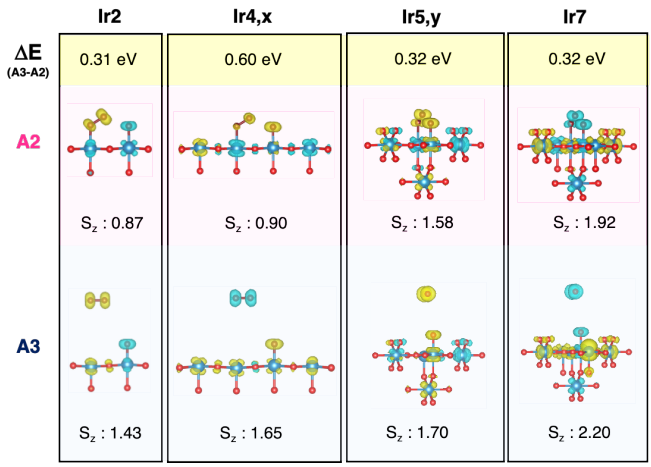

Figure 4. *Energy barrier and spin density with the spin number S_z for embedded clusters of A2 and A3 state at B3LYP-D3(BJ) level of theory. Isosurface 0.03 a.u. Color code: as Figure 3.*

In order to test how the A3-A2 energy difference and spin density depend on the DFT exchange correlation functional for the different cluster sizes, we have also examined using the B3LYP-D3(BJ) hybrid functional[36,37] (Figure 4). In close agreement with previous calculations on small IrO_2 cluster model[6] and the well-known O_2 under-binding by hybrid functional[19], energy barriers drop by ~0.7/0.8 eV for Ir2, Ir5,y and Ir7 clusters with respect to the PBE-D3(BJ) values, and by ~0.5 eV for the Ir4,x cluster. Analysis of the spin density (Figure 4) can explain this different behavior since the hybrid functional delivers a less stable A3 state with a high spin state on Ir atoms for Ir4,x. Noteworthy, the smallest cluster Ir2 gives the same ΔE results of largest Ir7 cluster. Overall, the energetics and electronic analysis (Table 1 and Figure 3, 4) indicate that the small cluster with 2 Ir atoms embedded by the large point charge array (exactly ~7100 point charges, Env-2 in Figure S4b), is the best choice to mimic the periodic IrO_2(110) surface at affordable computational costs. Therefore, we choose this model to investigate the oxygen release thermodynamic barrier (ΔE_{A3-A2}) by NEVPT2 calculations.

III. Oxygen release via electrostatic embedded approach: NEVPT2 energetics

A crucial step within the NEVPT2 approach is the choice of the active space CAS(e^-, MO), which must include all relevant orbitals of species involved in the process (Fig. S4a). Significant orbitals are listed hereunder:

- The O_2 molecular orbitals (MOs) given by the O 2s and 2p atomic orbitals, which are shown for completeness in Figure S4b.
- Due to the radical nature of Ir-oxo[4-7] and inspired by previous theoretical study on Fe-O binding[20], 4 orbitals are to be considered for the Ir-oxo species, namely the $2\pi_{dp}$ and $2\pi^*_{dp}$ orbitals (Fig. S4c). These orbitals arise from a bonding/antibonding π interaction of Ir d_{xz}, d_{yz} orbitals with p_x, p_y O atomic orbitals. Moreover, we find that the Ir-oxo π^*_{dpx} orbital is combined with the O_2 π^*_z MO upon molecular oxygen-Ir bonding (Ir_R), leading to bonding $(\pi^*_{dpx}\pi^*_z)$ and antibonding $(\pi^*_{dpx}\pi^*_z)^*$ orbitals (also shown in Fig. S4c).
- Considering the A2 species, we find that the O_2 π^*_y MO forms a non-covalent π interaction with Ir_R d_{yz} orbital, leading to the two orbitals $\pi_{d\pi y}$,$\pi^*_{d\pi y}$ depicted in Figure S4d. This metal-O_2 π interaction involve the donation of electron density from the filled metal d_{yz} orbital to the partially filled π^*_y orbital of oxygen molecule. Meanwhile, we find no significant metal-O_2 σ interaction between Ir_R d_{z^2} orbital and O_2 π^*_Z, probably because there is a favored interaction of latter with the Ir-oxo π^*_{dpx} orbital (Fig. S4c).

We start with the minimum active space with 4 electrons in 4 orbitals, CAS(4,4), which includes the $\pi_{d\pi y}$, $\pi^*_{d\pi y}$, $(\pi^*_{dpx}\pi^*_z)$ and $(\pi^*_{dpx}\pi^*_z)^*$ orbitals for the A2 state, and d_{yz} of Ir_R, π^*_y, π^*_z and π^*_{dpx} for A3. We also investigated larger active spaces (described in Figure S5 of SI) expanding to the largest CAS(18,13). This is built from the 4 ($2\pi_{dp}$ $2\pi^*_{dp}$) orbitals of Ir-oxo species, the 8 (σ_s σ^*_s 2π $2\pi^*$ σ_p σ^*_p) MOs of released O_2 and the d_{yz} orbital of Ir_R bound to O_2.

Within such active spaces, beginning with the smallest CAS(4,4), we can have up to four unpaired electrons. These are allocated to the $\pi_{d\pi y}$, $\pi^*_{d\pi y}$, $(\pi^*_{dpx}\pi^*_z)$ and $(\pi^*_{dpx}\pi^*_z)^*$ orbitals in A2 or to the π^*_{dpx} (Ir-Oxo), $2\pi^*$ (O_2) and d_{yz} (Ir_R) orbitals in A3. Beyond the radical nature of the Ir-oxo species[4-7], this feature suggests that both A2 and A3 can be found in three possible states with singlet, triplet, and quintet spin multiplicity, indicated as ^{1}A2, ^{3}A2, ^{5}A2 or ^{1}A3, ^{3}A3, ^{5}A3 for A2 and A3, respectively. In terms of relative electronic energies, we find that the ^{1}A2 is the ground state for all active spaces, while ^{1}A3, ^{3}A3 and ^{5}A3 are degenerate at both CASSCF and NEVPT2 (Figure S6 in SI) levels of theory, except for CAS(14,11), which predicts a singlet A3 state (^{1}A3) lying ~1.19 eV above both ^{3}A3 and ^{5}A3. The ^{1}A3 state can be linked to the first excited oxygen state, i.e. the singlet close shell ($^1O_2$: $^1\Delta_g$)[38]. This is confirmed by the occupation number of π^*_{O2} MOs, specifically (1.04, 1.04) and (1.99, 0.14) for (π^*_z, π^*_y) orbitals in $^{5/3}$A3 and ^{1}A3 states, respectively, as shown in Figure S7 of the SI.

Considering the target A2-A3 energy difference, the EEC[NEVPT2] approach predicts A3 at higher energy than A2, for all active spaces explored except for CAS(8,7), CAS(10,8), CAS(10,9) and CAS(12,10), where A3 is more stable than A2 (Figure S6b in SI). Detailed MOs analysis of these three active spaces (see Figure S5 in SI) reveals that CAS(10,8) and CAS(12,10) are different for A2 and A3, while CAS(10,9) includes the two σ_p σ^*_p MOs and not the 2π MOs of O_2. Concerning CAS(8,7), 6 MOs belong to the Ir-oxo species and 2 MOs to O_2. Therefore, this active space has more contribution from Ir-oxo rather than from the oxygen molecule. This suggests that the wrong A2-A3 order can be ascribed to an unbalanced representation of O_2 with respect to the Ir-oxo species. Overall, these results highlight that a reliable description of oxygen evolution requires considering balanced active spaces for the A2 and A3 species, including more MOs of the released oxygen molecule, in a similar fashion as in a free oxygen molecule, namely the π^*_{2p} π_{2p}, σ_{2p} σ^*_{2p}, and σ_{2s} σ^*_{2s} MOs (see Figure S7b). The necessity of incorporating all the molecular orbitals of oxygen molecules for an accurate description of the release reaction is already emphasized in a prior study.[39] If we exclude the aforementioned active spaces since they do not fulfil these conditions, the EEC[NEVPT2] energy barrier for oxygen release converges to ~0.8 eV at larger active spaces CAS(14,11) and CAS(18,13)

(Figure S8). The fulfillment of a converged energy barrier reaffirms the appropriateness of the chosen active space.

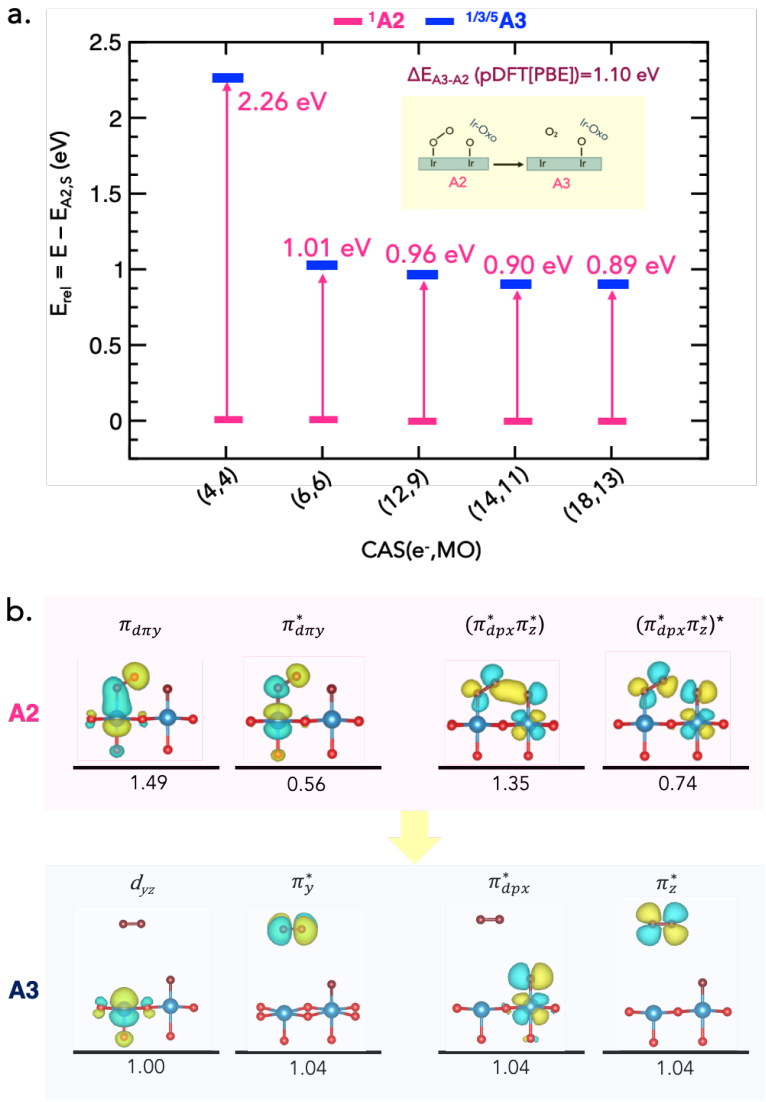

Figure 5. a) *Energy difference for oxygen evolution (A2 →A3) by pDFT:NEVPT2 hybrid scheme (eq. 4). The active spaces are named CAS(n,m), where n and m are the number of electrons and orbitals, respectively.* ***b)*** *Significative MOs in the active spaces with their occupation numbers for CAS(18e,13o). Energetic color code: ^{1}A2 (magenta); the degenerate ^{1}A3, ^{3}A3 and ^{5}A3 (blue). Atomic color code: as in Figure 1, isodensity surfaces (0.03 a.u.) are depicted as yellow and cyan for positive and negative values, respectively.*

Due to the IrO_2 metallic nature with long range entanglement in the wave function, and the error for finite embedded cluster size, we correct the periodic DFT (pDFT) energies based on the difference between the EEC[NEVPT2] and EEC[PBE] calculations on the same embedded cluster. Thus, we define a hybrid pDFT:NEVPT2 energy via a subtractive scheme[40,41]:

$$E_{pDFT:NEVPT2} = E_{pDFT[PBE]} - E_{EEC[PBE]} + E_{EEC[NEVPT2]} \quad (4)$$

where $E_{pDFT[PBE]}$ is the energy computed via periodic DFT with the PBE-D3(BJ) functional, while $E_{EEC[PBE]}$ and $E_{EEC[NEVPT2]}$ are the energies computed via the electrostatic embedded approach at PBE-D3(BJ) and NEVPT2 level of theory, respectively. The $\Delta E_{\text{A3-A2}}$ energy differences computed via this pDFT:NEVPT2 approach are showed in Figure 5.

The converged pDFT:NEVPT2 $\Delta E_{\text{A3-A2}}$ energy difference (~0.90 eV) is ~0.2 eV lower than the pDFT[PBE] one (1.10 eV). If we apply an energy correction of ~0.4 eV to (ΔE to obtain (ΔG, mirroring results from a previous theoretical work $(\Delta G_{A3-A2}(pDFT[PBE]) = 0.56/0.58\ eV\ vs\ \Delta E_{A3-A2}(pDFT[PBE]) \approx 1.00\ eV$ accounting for the effects of solvation, zero-point energy (ZPE), enthalpy and entropy contributions)[6], the multireference method predicts a free energy difference $\Delta G_{A3-A2} \approx 0.45/0.47\ eV$, a value close to the reference microkinetic value ($\Delta G_{A3-A2} = 0.43\ eV$).[12] The interaction between O_2 and IrO_2 surface in A2 primarily involves the $\pi_{d\pi y}$, $\pi^*_{d\pi y}$, $(\pi^*_{dpx}\pi^*_z)$ and $(\pi^*_{dpx}\pi^*_z)^*$ orbitals (Figure 2b); this holds true not only for CAS(18,13) but also for all active spaces explored (see Figure S8). When O_2 is released (A3), our calculations suggest that the $\Delta E_{\text{A3-A2}}$ energy difference arises from two vanished interactions: the breaking of a π interaction between O_2 and Ir surface atom, and a further interaction with adjacent electrophilic Ir-oxo species present at the experimental operating conditions.[6] Different occupation and shape of the MOs are found at PBE-D3(BJ) level of theory (Figure S11). With a smaller contribution from the Ir-oxo π^*_{dpx} orbital, the A2 $(\pi^*_{dpx}\pi^*_z)$ and $(\pi^*_{dpx}\pi^*_z)^*$ orbitals are more delocalized over the whole cluster. Plus, analysis on the A3 DFT-PBE molecular orbitals, the π^*_{dpx} is totally unoccupied, while two electrons occupy the Ir d_{yz} orbitals. These results suggest that the DFT-PBE approach poorly describes the

radical character of the Ir-oxo species. This also can explain the slight decrease of the energy barrier within the multireference approach.

With a smaller contribution from the Ir-oxo d orbital, the A2 ($\pi^*_{dpx}\pi^*_z$) and ($\pi^*_{dpx}\pi^*_z$)* orbitals are more delocalized over the whole cluster. The DFT-PBE technique inadequately predicts the radical character of the Ir-oxo species because the two electrons lost by the liberated oxygen molecule are localized on the Ir d orbitals.

CONCLUSIONS

Remarkable experimental and theoretical progresses provide several insights on the OER mechanism at IrO_2 interfaces: a crucial feature is the removal of the molecular oxygen from the catalyst surface, a rather high energy barrier for this process has been identified by an experimentally derived microkinetic model. Unveiling the origin of such crucial step represents a challenging task. Standard semi-local DFT predict too high O_2-release barrier because of the well-known over-binding of molecular oxygen to transition metal oxide surface.

Therefore, we present for the first-time a thorough investigation on such oxygen release at the IrO_2(110) interface to dissect the nature of the O_2-release barrier, comparing the widely used periodic DFT with the multireference NEVPT2-embedded approach. With periodic PBE-D3(BJ) we find a local energy minimum after oxo-oxo coupling in the I2M, a Ir-O cleavage, and further water adsorption. From such minimum, water oxidation leads to the same evolving O_2 steps as those of the AEM path, which is the most likely scenario.

As in previous works[6,12], the PBE-D3(BJ) level of theory predicts a high energy barrier (~1.10 eV) for dioxygen release via the AEM path. Because this step involves radical Ir-oxo specie and triplet O_2, multireference methods by means of an electrostatic embedded method are used to provide a reliable electronic description of this process. First, we validate this method analyzing different clusters and charge arrays of increasing size at PBE-D3(BJ) level of theory. Energetic and electronic analysis reveals that the smaller cluster with 2 Ir atoms with the largest charge array is the best choice to mimic the periodic

IrO_2(110) surface at affordable computational costs. With this cluster-embedded model at the CASSCF/NEVPT2 level of theory, when O_2 is bound to surface (A2), the ground state has a singlet spin multiplicity, while when it is released (A3), the singlet, triplet and quintet (^{1}A3, ^{3}A3 and ^{5}A3, respectively) states are degenerate. Concerning the active spaces, a reliable description of this AEM step is only achieved when a consistent active space is employed for the two system, A2 and A3, including all the valence O_2 MOs, namely the π^*_{2p}, π_{2p}, $\sigma_{2\mathrm{p}}$, $\sigma^*_{2\mathrm{p}}$, $\sigma_{2\mathrm{s}}$ and $\sigma^*_{2\mathrm{s}}$ orbitals. Furthermore, large active spaces, not less than 14 MOs and 11 electrons (CAS(14,11)), including MOs of adjacent Ir-oxo specie, are required for the convergence to the final dioxygen release energy barrier. While the DFT-PBE approach provides a high value ($\Delta G_{A3-A2} \approx 0.56/0.58\ eV$)[6,12], the activation energy at pDFT:NEVPT2 level of theory ($\Delta G_{A3-A2} \approx 0.45/0.47\ eV$) is consistent with the experimentally derived microkinetic value ($\Delta G_{A3-A2} \approx 0.43\ eV$).[12] By analysis of the active orbitals, such a barrier can be ascribed to the breaking of a π interaction between O_2 and Ir surface atom, and of a further interaction with adjacent electrophilic Ir-oxo species, present at the experimental operating condition.

It is worth noting that our model lack of solvent and electrolyte. The influence of electrode charging, solvent, and electrolyte ions on the reaction mechanism can be critical for a comprehensive study of electrocatalysis. However, the agreement between our pDFT:NEVPT2 energy barrier and the microkinetic result, which takes into account both theoretical and experimental data,[12] reinforces the relevance of our model in approximating real-system behavior.

Beyond the specific results, this study validates a feasible multireference embedded cluster approach for electrocatalysis, thus paving the route to future applications of such approach to complex reactions at strongly correlated heterogeneous interfaces. Meanwhile our work aims to understand the multi-reference nature and overcome the challenges of accurate energy barrier estimation for the OER at IrO_2 interfaces, we recognize the need to explore effects of other factors, e.g. solvents, electrolyte or also other surface facets and the need to expand our analysis to other catalysts, which further investigations will provide a

more comprehensive understanding of OER mechanisms, how they vary across different catalyst materials and a strategy to design and optimize new catalysts.

CONFLICT OF INTERESTS

The authors have no conflicts of interest to declare.

ACKNOWLEDGMENTS

This article was based upon a work by COST Action 18234, supported by COST (European Cooperation in Science and Technology). The authors also acknowledge COST Action 18234 for supporting a Short-Term Scientific Mission (STSM). This work was partially supported by the Catalyst Design for Decarbonization Center, an Energy Frontier Research Center funded by the U.S. Department of Energy, Office of Science, Basic Energy Sciences under Award No. DE-SC0023383. Computer resources were provided by the Research Computing Center at the University of Chicago.

SUPPORTING INFORMATION

Supplementary Material is available online and contains structural model for (110) IrO_2 surface and embedded clusters for method validations. Periodic DFT energetics, electronic analysis on A2 and A3 states, molecular orbitals scheme and EEC[CASSCF] and EEC[NEVPT2] energetics.

REFERENCES

1. Wu, H.; Wang, Y.; Shi, Z.; Wang, X.; Yang, J.; Xiao, M.; Ge, J.; Xing, W.; Liu, C. Recent Developments of Iridium-Based Catalysts for the Oxygen Evolution Reaction in Acidic Water Electrolysis. Journal of Materials Chemistry A, 2022, 10, 13170–13189.
2. Lončar, A.; Escalera-López, D.; Cherevko, S.; Hodnik, N. Inter-relationships between Oxygen Evolution and Iridium Dissolution Mechanisms. Angewandte Chemie International Edition, 2022, 61.

3. Naito, T.; Shinagawa, T.; Nishimoto, T.; Takanabe, K. Recent Advances in Understanding Oxygen Evolution Reaction Mechanisms over Iridium Oxide. Inorganic Chemistry Frontiers, 2021, 8, 2900–2917.
4. Pfeifer, V.; Jones, T. E.; Velasco Vélez, J. J.; Arrigo, R.; Piccinin, S.; Hävecker, M.; Knop-Gericke, A.; Schlögl, R. In Situ Observation of Reactive Oxygen Species Forming on Oxygen-Evolving Iridium Surfaces. Chemical Science, 2017, 8, 2143–2149.
5. Saveleva, V. A.; Wang, L.; Teschner, D.; Jones, T.; Gago, A. S.; Friedrich, K. A.; Zafeiratos, S.; Schlögl, R.; Savinova, E. R. Operando Evidence for a Universal Oxygen Evolution Mechanism on Thermal and Electrochemical Iridium Oxides. The Journal of Physical Chemistry Letters, 2018, 9, 3154–3160.
6. Ping, Y.; Nielsen, R. J.; Goddard, W. A., III. The Reaction Mechanism with Free Energy Barriers at Constant Potentials for the Oxygen Evolution Reaction at the IrO_2 (110) Surface. Journal of the American Chemical Society, 2016, 139, 149–155.
7. Velasco-Vélez, J.-J.; Carbonio, E. A.; Chuang, C.-H.; Hsu, C.-J.; Lee, J.-F.; Arrigo, R.; Hävecker, M.; Wang, R.; Plodinec, M.; Wang, F. R.; Centeno, A.; Zurutuza, A.; Falling, L. J.; Mom, R. V.; Hofmann, S.; Schlögl, R.; Knop-Gericke, A.; Jones, T. E. Surface Electron-Hole Rich Species Active in the Electrocatalytic Water Oxidation. Journal of the American Chemical Society, 2021, 143, 12524–12534.
8. Zagalskaya, A.; Alexandrov, V. Role of Defects in the Interplay between Adsorbate Evolving and Lattice Oxygen Mechanisms of the Oxygen Evolution Reaction in RuO_2 and IrO_2. ACS Catalysis, 2020, 10, 3650–3657.
9. González, D.; Heras-Domingo, J.; Sodupe, M.; Rodríguez-Santiago, L.; Solans-Monfort, X. Importance of the Oxyl Character on the IrO_2 Surface Dependent Catalytic Activity for the Oxygen Evolution Reaction. Journal of Catalysis, 2021, 396, 192–201.

10. Camacho-Forero, L. E.; Godínez-Salomón, F.; Ramos-Sánchez, G.; Rhodes, C. P.; Balbuena, P. B. Theoretical and Experimental Study of the Effects of Cobalt and Nickel Doping within IrO_2 on the Acidic Oxygen Evolution Reaction. Journal of Catalysis, 2022, 408, 64–80.
11. Schweinar, K.; Gault, B.; Mouton, I.; Kasian, O. Lattice Oxygen Exchange in Rutile IrO_2 during the Oxygen Evolution Reaction. The Journal of Physical Chemistry Letters, 2020, 11, 5008–5014.
12. Geppert, J.; Röse, P.; Czioska, S.; Escalera-López, D.; Boubnov, A.; Saraçi, E.; Cherevko, S.; Grunwaldt, J.-D.; Krewer, U. Microkinetic Analysis of the Oxygen Evolution Performance at Different Stages of Iridium Oxide Degradation. Journal of the American Chemical Society, 2022, 144, 13205–13217.
13. Zagalskaya, A.; Evazzade, I.; Alexandrov, V. Ab Initio Thermodynamics and Kinetics of the Lattice Oxygen Evolution Reaction in Iridium Oxides. ACS Energy Letters, 2021, 6, 1124–1133.
14. Perdew, J. P.; Burke, K.; Ernzerhof, M. Generalized Gradient Approximation Made Simple. Physical Review Letters, 1996, 77, 3865–3868.
15. Perdew, J. P.; Burke, K.; Ernzerhof, M. Generalized Gradient Approximation Made Simple [Phys. Rev. Lett. 77, 3865 (1996)]. Physical Review Letters, 1997, 78, 1396–1396.
16. Angeli, C.; Cimiraglia, R.; Evangelisti, S.; Leininger, T.; Malrieu, J.-P. Introduction ofn-Electron Valence States for Multireference Perturbation Theory. The Journal of Chemical Physics, 2001, 114, 10252–10264.
17. Perdew, J.P.; Schmidt, K. Density Functional Theory and its Application to Materials, edited by Doren, V. van, Alsenoy, C. van, and Geerlings, P. (American Institute of Physics, Melville, NY, 2001).
18. Sargeant, E.; Illas, F.; Rodríguez, P.; Calle-Vallejo, F. Importance of the Gas-Phase Error Correction for O_2 When Using DFT to Model the Oxygen Reduction and Evolution Reactions. Journal of Electroanalytical Chemistry, 2021, 896, 115178.

19. Radoń, M.; Pierloot, K. Binding of CO, NO, and O_2 to Heme by Density Functional and Multireference Ab Initio Calculations. The Journal of Physical Chemistry A, 2008, 112, 11824–11832.
20. Kurashige, Y.; Saitow, M.; Chalupský, J.; Yanai, T. Radical O–O Coupling Reaction in Diferrate-Mediated Water Oxidation Studied Using Multireference Wave Function Theory. Phys. Chem. Chem. Phys., 2014, 16, 11988–11999.
21. Kunz, A.b. Embedded cluster methods for surface and chemisorption studies. Surface Science 1987, 26, 165-174.
22. Liao, P.; Carter, E.A. Optical Excitations in Hematite (α-Fe_2O_3) via Embedded Cluster Models: A CASPT2 Study. J. Phys. Chem. C 2011, 115, 20795-20805.
23. Teusch, T.; Klüner, T. Photodesorption Mechanism of Water on WO_3(001) – a Combined Embedded Cluster, Computational Intelligence and Wave Packet Approach. Phys. Chem. Chem. Phys. 2020, 22, 19267–19274.
24. Gerhards, L.; Klüner, T. Theoretical Investigation of CH-Bond Activation by Photocatalytic Excited SO_2 and the Effects of C-, N-, S-, and Se-Doped TiO_2. Phys. Chem. Chem. Phys. 2022, 24, 2051–2069.
25. Kubas, A.; Berger, D.; Oberhofer, H.; Maganas, D.; Reuter, K.; Neese, F. Surface Adsorption Energetics Studied with "Gold Standard" Wave-Function-Based Ab Initio Methods: Small-Molecule Binding to TiO_2 (110). J. Phys. Chem. Lett. 2016, 7, 4207–4212.
26. Giannozzi, P.; Baseggio, O.; Bonfà, P.; Brunato, D.; Car, R.; Carnimeo, I.; Cavazzoni, C.; de Gironcoli, S.; Delugas, P.; Ferrari Ruffino, F.; Ferretti, A.; Marzari, N.; Timrov, I.; Urru, A.; Baroni, S. Quantum ESPRESSO toward the Exascale. The Journal of Chemical Physics, 2020, 152, 154105.
27. Grimme, S.; Antony, J.; Ehrlich, S.; Krieg, H. A Consistent and Accurate Ab Initio Parametrization of Density Functional Dispersion Correction (DFT-D) for the 94 Elements H-Pu. The Journal of Chemical Physics, 2010, 132, 154104.

28. Blöchl, P. E. Projector Augmented-Wave Method. Physical Review B, 1994, 50, 17953–17979.
29. Dal Corso, A. Pseudopotentials Periodic Table: From H to Pu. Computational Materials Science, 2014, 95, 337–350.
30. Marzari, N.; Vanderbilt, D.; De Vita, A.; Payne, M. C. Thermal Contraction and Disordering of the Al(110) Surface. Physical Review Letters, 1999, 82, 3296–3299.
31. Sun, W.; Ceder, G. Efficient creation and convergence of surface slabs. Surf. Sci. 2013, 617, 53–59 .
32. Marzari, N.; Vanderbilt, D.; De Vita, A.; Payne, M. C. Thermal Contraction and Disordering of the Al(110) Surface. Physical Review Letters, 1999, 82, 3296–3299.
33. Matz, O.; Calatayud, M. Periodic DFT Study of Rutile IrO_2: Surface Reactivity and Catechol Adsorption. The Journal of Physical Chemistry C, 2017, 121, 13135–13143.
34. Neese, F.; Wennmohs, F.; Becker, U.; Riplinger, C. The ORCA Quantum Chemistry Program Package. The Journal of Chemical Physics, 2020, 152, 224108.
35. Hay, P. J.; Wadt, W. R. Ab Initio Effective Core Potentials for Molecular Calculations. Potentials for K to Au Including the Outermost Core Orbitals. The Journal of Chemical Physics, 1985, 82, 299–310.
36. Becke, A. D. J. Density-functional thermochemistry. III. The role of exact exchange. Chem. Phys. 1993, 98, 5648−5652.
37. Lee, C.; Yang, W.; Parr, R. G. Development of the Colle-Salvetti correlation-energy formula into a functional of the electron density. Phys. Rev. B 1988, 37, 785−789.
38. Ogilby, P. R. Singlet Oxygen: There Is Indeed Something New under the Sun. Chemical Society Reviews, 2010, 39, 3181.
39. Fasulo, F.; Massaro, A.; Muñoz-García, A. B.; Pavone, M. New Insights on Singlet Oxygen Release from Li-Air Battery Cathode: Periodic DFT Versus CASPT2 Embedded Cluster Calculations. Journal of Chemical Theory and Computation, 2023, 19, 5210–5220.

40. Sauer, J. Ab Initio Calculations for Molecule–Surface Interactions with Chemical Accuracy. Accounts of Chemical Research, 2019, 52, 12, 3502–3510.
41. Chung, L. W.; Sameera, W. M. C.; Ramozzi, R.; Page, A. J.; Hatanaka, M.; Petrova, G. P.; Harris, T. V.; Li, X.; Ke, Z.; Liu, F.; Li, H.-B.; Ding, L.; Morokuma, K. The ONIOM Method and Its Applications. Chemical Reviews, 2015, 115, 5678–5796.
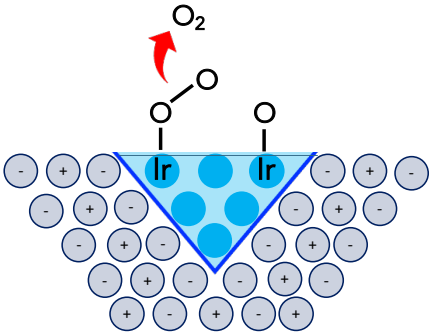
For Table of Contents